MIT Libraries | DSpace@MIT

MIT Open Access Articles

An Evaluation of Hurricane Superintensity in Axisymmetric Numerical Models

Massachusetts Institute of Technology

An Evaluation of Hurricane Superintensity in Axisymmetric Numerical Models

RAPHAËL ROUSSEAU-RIZZI AND KERRY EMANUEL

*Lorenz Center, Department of Earth, Atmospheric and Planetary Sciences,
Massachusetts Institute of Technology, Cambridge, Massachusetts*

ABSTRACT

Potential intensity (PI) is an analytical bound on steady, inviscid, axisymmetric hurricane wind speed. Studies have shown that simulated hurricane azimuthal wind speed can greatly exceed a PI bound on the maximum gradient wind. This disparity is called superintensity (SI) and has been attributed to the contribution of the unbalanced flow to the azimuthal wind. The goals of this study are 1) to introduce a new surface wind PI (PI_s), based on a differential Carnot cycle and bounding the magnitude of the surface winds; 2) to evaluate SI in numerical simulations with respect to diagnostic PI bounds on gradient wind (PI_g), azimuthal wind (PI_a), and surface wind (PI_s); and 3) to evaluate the validity of each PI bound based on the SI computations. Here, we define superintensity as the normalized amount by which each version of PI is exceeded by the quantity it bounds. Axisymmetric tropical cyclone simulations are performed while varying the parameterized turbulent mixing as a way of estimating SI in the inviscid limit. As the mixing length decreases, all three bounded wind speeds increase similarly from a sub-PI state to a marginally superintense state. This shows that all three forms of PI evaluated here are good approximations to their respective metrics in numerical simulations.

1. Introduction

a. Definition and relevance of superintensity

Tropical cyclones (TCs), or hurricanes, are the single most destructive natural disaster in the United States, with a cumulative damage cost of \$265 billion for 2017 alone (Office For Coastal Management 2018). While our ability to forecast hurricane intensity (wind speed) has generally improved along with track forecasting, over the last 25 years, 24-h lead-time forecast skill has improved very slowly (DeMaria et al. 2014). In addition, it has been hypothesized that the forecasting of TC intensity with climate change will become more difficult as the intensification rates are expected to increase (Emanuel 2017).

TCs are a complex phenomenon, and, while our understanding of the underlying physics has made large and regular progress over the last three decades, discrepancies remain between analytical theories,

numerical models, and observations. In that context, we must strive to reconcile analytical hurricane intensity theories with both hurricane data and numerical simulations. This is a necessary step in understanding the mechanisms of intensification and improving forecast models.

Analytical theories for hurricane intensity include the concept of potential intensity (PI), a theoretical upper bound on inviscid, steady-state, and axisymmetric hurricane wind speed. PI can be defined to bound various quantities such as the gradient wind (Emanuel 1986), the azimuthal wind (Bryan and Rotunno 2009a, hereafter BR09a), and the magnitude of the surface winds (Bister and Emanuel 1998). Each form of PI can be considered to represent a different simplified picture of the relation between the TC dynamics and thermodynamics.

Gradient wind balance is defined as the state in which the Coriolis and centrifugal accelerations balance the pressure gradient acceleration in the radial momentum equation; that is, the system is in steady state and the diffusive and advective terms are negligible. Under the assumption that TCs are in gradient wind balance, gradient wind PI (PI_g, arguably the most widespread PI theory) should also bound the maximum azimuthal winds for any given storm. And indeed, gradient wind PI has been shown to be generally well respected in

---

Corresponding author: Rousseau-Rizzi, rrizzi@mit.edu

nature (Emanuel 2000). However, the maximum azimuthal wind speeds within a few strong storms have been observed to exceed the PI_g bound (Montgomery et al. 2006).

One of the main inconsistencies between numerical models and analytical theories that has been discussed in the literature is called superintensity (Persing and Montgomery 2003). Superintensity (SI) as defined by Persing and Montgomery (2003) occurs when the maximum steady-state azimuthal wind speed of a tropical cyclone exceeds the gradient wind potential intensity, sometimes greatly. An alternative definition of SI will be introduced and used later in this paper. Superintensity has mostly been studied in axisymmetric numerical models, which are easier to use and compare more directly to PI theory than 3D numerical models.

In a sensitivity study, Hausman (2001) noticed that increasing the resolution in axisymmetric hurricane models was associated with azimuthal wind speed increasing beyond observed values for a similar environment. The subsequent study by Persing and Montgomery (2003) sought to understand this discrepancy, and, noting that the simulated winds well exceeded PI_g, they coined the term superintensity. Their explanation, that the import of high entropy air from the eye into the eyewall was responsible for the high intensity, was later shown by Bryan and Rotunno (2009b, hereafter BR09b) not to be the dominant factor in SI. The work on SI by Bryan and Rotunno is very relevant to this study.

Using Cloud Model 1 (CM1) (Bryan and Fritsch 2002), BR09a showed hurricane intensity (and superintensity) to be very sensitive to the parameterized mixing of enthalpy and momentum. Other studies with CM1, including Bryan and Rotunno (2009c, hereafter BR09c), Rotunno and Bryan (2012), and Bryan (2012) found that the intensity of simulated axisymmetric TCs increased significantly with decreasing horizontal mixing length l_h. The mixing length influences the magnitude of the horizontal mixing following the parameterization introduced in Rotunno and Emanuel (1987, hereafter RE87) axisymmetric TC model and based on the Smagorinsky (1963) turbulence parameterization. Keeping the environment and all other parameters fixed, BR09a found that decreasing l_h from values of about 3000 to 125 m increases the TC azimuthal wind from less than PI_g to 150% of PI_g. Note that, according to the PI assumption of inviscid flow, the intensity of the simulated TCs should converge to PI when l_h decreases, and not exceed it. The sensitivity of azimuthal wind to l_h can be likened to the sensitivity to resolution reported by Hausman (2001). Indeed, lower mixing and, to a certain extent, higher resolution are

both associated with stronger radial gradients of entropy, and thus intensity.

BR09a found the gradient wind balance assumption in the gradient PI (PI_g) theory to be clearly violated in their simulations. This means that superintensity of the azimuthal winds with respect to the gradient wind PI (PI_g) occurs because of gradient wind imbalance, namely, supergradient flow. Using methods by D. K. Lilly (unpublished manuscript) and Bister and Emanuel (1998), BR09a derived a PI expression based on both thermodynamic and dynamic diagnostics to account for the contribution of unbalanced winds in PI. This expression provides a good upper bound on the azimuthal wind (called PI+ in BR09a and PI_a hereafter). While bounds on the gradient wind can be computed a priori, from the environment alone, including agradient winds makes it very difficult to bound the azimuthal wind from the environment only, so that it can only be evaluated diagnostically.

To summarize, BR09a show that, in the early studies of Hausman (2001) and Persing and Montgomery (2003), SI was largely due to supergradient effects. They then explain why PI_g seems to work in constraining the observed azimuthal winds of tropical cyclones.

Willoughby (1990) showed that the azimuthal mean winds of certain observed TCs are very close to gradient wind balance above the frictional layer. This agrees with Emanuel's (1986) assumption of thermal wind balance above the boundary layer, but not with simulations, if we assume that the TCs are inviscid. BR09a reconcile this disparity by pointing out that the TCs are indeed not inviscid and that horizontal mixing tends to weaken the storm and favor gradient wind balance. Three-dimensional turbulence has been shown to become important in intense storms, which limits the increase in mean azimuthal wind velocity (e.g., Rotunno et al. 2009; Yang et al. 2007; Brown and Hakim 2013). However, even with an increase in three-dimensional turbulent mixing, some storms are observed to have winds that are supergradient by up to $10 \, \mathrm{m \, s^{-1}}$ (Kepert 2006), which could explain the observed superintensity.

To summarize, studies evaluating PI have done so for gradient wind PI and azimuthal wind PI in low-mixing environments. The PI_g bound was shown not to work very well for azimuthal winds and for small mixing lengths, but to work well for gradient winds, outlining the fact that TC intensities should be compared to the appropriate PI bound. Hereafter, SI will be defined as the discrepancy between a given form of PI and the numerically simulated intensity it bounds, and will be used to evaluate various PI theories in the same simulations.

Generally, SI in numerical models implies that there is a limitation either with the PI bound or with the way hurricanes are represented in current models. In this study, we will use SI to evaluate the different representations of the TC physics associated with various forms of PI, assuming that the contribution from numerical errors is negligible. The possible contribution of model numerics or parameterizations to SI is deferred to a future study.

b. New and existing forms of PI

This study aims to evaluate both new and existing forms of PI in numerical simulations. Section 2 of this paper introduces a new derivation (briefly described in Emanuel 2018) for a PI bound on the maximum surface winds, similar to the one derived in Bister and Emanuel (1998). This new surface PI (PI$_s$) is derived with as few assumptions as possible, using the concept of a differential Carnot cycle. It provides a thermodynamic bound on the magnitude of the surface winds including the radial inflow component. The expressions for gradient wind PI and azimuthal wind PI introduced, respectively, by Emanuel (1986) and BR09a will be evaluated as well. A short derivation of these two forms follows, while the third, new form is derived in section 2.

c. Gradient wind PI

The most widely used analytical model of hurricane energetics was first published in Emanuel (1986). This steady-state, inviscid, axisymmetric model provides the basis of what is now called potential intensity using 1) the assumption of moist slantwise neutrality, 2) the assumption of thermal wind balance (hydrostatic and gradient wind balance combined), and 3) a boundary layer closure. The gradient wind V_g is defined as the azimuthal wind required so that the sum of the Coriolis and centrifugal accelerations balance the radial pressure gradient acceleration. Assuming moist slantwise neutrality is equivalent to assuming that the angular momentum M surfaces coincide with the saturation entropy s^* surfaces, neglecting the direct contribution of variable water content to density. The angular momentum is given by $M = Vr + 1/2 fr^2$, where V is the azimuthal velocity (here, $V = V_g$), r is the radius, and f is a constant Coriolis parameter. In Emanuel (1986), the thermal wind relation is given by

$$\frac{1}{r^3}\left(\frac{\partial M^2}{\partial p}\right)_r = -\left(\frac{\partial T}{\partial p}\right)_{s^*}\left(\frac{\partial s^*}{\partial r}\right)_p, \quad (1)$$

where the subscripts denote quantities being held constant. Moist slantwise neutrality allows us to integrate Eq. (1) upward along surfaces of constant angular

momentum, between the top of the boundary layer and the outflow, defined as the point where the azimuthal velocity vanishes. This yields

$$\frac{V_{g,b}}{r_b} = -\frac{ds^*}{dM}(T_b - T_{out}), \quad (2)$$

where subscript b denotes the top of the boundary layer and subscript "out" denotes the outflow layer. Equation (1) indicates that the vertical shear is monotonic with T so that the maximum velocity occurs at the top of the boundary layer. This means that $V_{g,b}$ is an upper bound on the gradient wind. From there, ds^*/dM has to be defined to get a diagnostic equation for maximum velocity. The boundary layer (BL) closure states that ds/dM in the BL is the ratio of the surface fluxes of entropy F_s and angular momentum $\bar{r}\tau_\theta$. Further, $ds^*/dM = ds/dM$ at the top of the BL, so that

$$\frac{ds^*}{dM} = \frac{F_s}{\bar{r}\tau_\theta}, \quad (3)$$

where $\bar{r}$ is the vertically averaged radius of angular momentum surfaces. We need to account for dissipative heating in the boundary layer because the inviscid assumption is only applied to the interior flow, and because the numerical models used in this study include dissipative heating parameterizations. We obtain

$$F_s = \frac{\rho}{T_s}[C_{k10}|\mathbf{V}_{10}|(k_s^* - k_{10}) + C_{D10}|\mathbf{V}_{10}|^3], \quad (4)$$

$$\tau_\theta = -\rho C_{D10}|\mathbf{V}_{10}|V_{10}. \quad (5)$$

In these equations, the subscript 10 designates the near-surface layer at 10 m above the air–sea interface; $|\mathbf{V}_{10}|$ is the magnitude of the surface winds; C_{k10} and C_{D10} are the bulk aerodynamic flux coefficients for enthalpy and momentum; $k = (c_p + q_t c_l)T + L_v q$ is the enthalpy, where q is the water vapor mixing ratio and q_t is the total water mixing ratio; and k_s^* is the saturation enthalpy at sea surface temperature T_s. We note that, for adiabatic and hydrostatic transformations, the enthalpy difference $(k_s^* - k_{10})$ is equivalent to the moist static energy (MSE) difference $(h_s^* - h_b)$ between the top of the boundary layer h_b and the surface temperature saturated state h_s^*. The MSE is given by $h = k + (1 + q_t)gz$. Next, Eqs. (3)–(5) are substituted into Eq. (2). Assuming that the radius of the angular momentum surfaces is similar at the top and at the bottom of the boundary layer, we get

$$V_{g,b} = \frac{1}{V_{10}}\frac{r_b}{\bar{r}}\frac{(T_b - T_{out})}{T_s}\left[\frac{C_{k10}}{C_{D10}}(k_s^* - k_{10}) + |\mathbf{V}_{10}|^2\right]. \quad (6)$$

Then, following Bister and Emanuel (1998), we assume that the momentum near the surface equals that at the top of the boundary layer ($V_{10} \approx V_{g,b}$, and $\bar{r} \approx r_b$), that $T_s \approx T_b$, and finally, that the dissipative heating effects can be properly captured by setting $|\mathbf{V}_{10}|^2 \approx V_{g,b}^2$. These assumptions allow us to simplify the equation further and obtain

$$\text{PI}_g^2 = V_{g,b}^2 = \frac{C_{k10}}{C_{D10}} \frac{(T_b - T_{\text{out}})}{T_{\text{out}}} (k_s^* - k_{10}), \qquad (7)$$

where we have redefined $V_{g,b}$ as PI_g, which denotes a potential intensity derived from dynamical principles, that represents an upper bound on gradient wind V_g. The validity of the simplifying approximations will be evaluated in the results section.

d. Azimuthal wind PI

Using the same boundary layer closure assumptions as in the PI_g derivation, along with the assumption that $M_b \approx V_b r_b$ in the inner core, the BR09a equation that accounts for the supergradient contribution is written

$$\text{PI}_a^2 = V_{\text{max}}^2 = \text{PI}_g^2 + r_b \eta_b w_b \frac{T_s}{T_o}, \qquad (8)$$

where r_b, η_b, and w_b are the radius, the azimuthal vorticity, and the vertical velocity at the location of maximum winds. Here, PI_a represents a bound on the maximum azimuthal wind.

e. Objectives

In summary, the main purpose of this study is to introduce a new derivation for surface PI (PI_s), based on the idea of a differential Carnot cycle and bounding the magnitude of the surface winds, and to evaluate this theory along with previous PI theories bounding the azimuthal winds and the gradient winds, by comparing them to numerically simulated values.

First, section 2 introduces the derivation of the surface PI based on a differential Carnot engine view of the TC. Then section 3 presents the model and simulation setup to investigate SI, and section 4 shows the results of these computations. Finally, section 5 compares the degree of superintensity for all forms of PI and all simulations.

2. Surface PI

The energy cycle of a hurricane can be described in terms of a Carnot heat engine (Emanuel 1986; Pauluis and Zhang 2017; Emanuel 2018), which provides an integral constraint on the maximum surface winds. Here, we derive a local constraint by differentiating

two adjacent cycles as shown in Fig. 1. The advantage of using a differential Carnot cycle instead of approximating the secondary circulation of the hurricane as a full Carnot cycle is twofold. First, it provides an expression for the maximum surface winds rather than an integral constraint on the surface winds for the whole storm. Second, it does not require the entire secondary circulation of the hurricane to satisfy the Carnot cycle's assumptions, but only the portion of the cycle located in the eyewall. Hakim (2011) showed that the secondary circulation of a simulated axisymmetric TC corresponds approximately to a Carnot cycle in the inflow and in the eyewall, but not in the outflow and subsidence regions.

In Fig. 1, cycle 1 begins at point A very near the surface in the boundary layer far outside the core and follows the spiraling inflow to point B incrementally inside the radius of maximum winds. This leg is approximated as isothermal, with strong input of enthalpy from the ocean and strong dissipation of kinetic energy. From B, the cycle follows air upward in the eyewall, and outward to point C, far outside the storm center; this leg is approximated as moist adiabatic and at constant energy and angular momentum. From point C, air sinks to point D while losing entropy and energy owing to radiative cooling; point D is chosen as a point in the environment that has the same moist entropy as point A. Leg C–D is approximated as isothermal, and angular momentum is regained along this leg, presumably owing to irreversible mixing. From D, the parcel sinks at constant angular momentum back to point A. In the upper part of this leg, air loses entropy though radiative cooling, but regains it through irreversible mixing as it approaches A. Cycle 2 is identical to cycle 1 except that the air turns upward in the eyewall at point B′ just outside the radius of maximum winds, and follows a streamline and angular momentum surface to point C' just under point C, but then sinking to point D and back to its starting point A. We can take points A and D to be the same in each cycle because they are in regions of very weak spatial gradients of entropy and angular momentum. Both legs B–C and B′–C′ are considered to occur at water saturation. A Carnot-like relationship between entropy gained in A–B (and lost in C–D) and mechanical dissipation can be derived from equations for conservation of moist entropy s and energy. We begin with by differentiating (following a parcel) the reversible moist entropy using its definition in Emanuel (1994):

$$T \frac{ds}{dt} = (c_{pd} + c_l q_t) \frac{dT}{dt} + \frac{d(L_v q)}{dt} - (1 + q_t)\alpha \frac{dp}{dt}$$
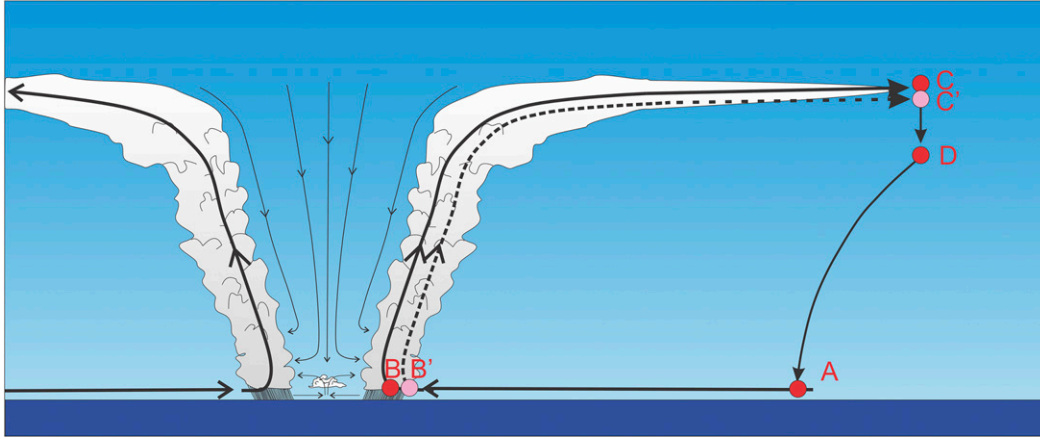$$- R_v T \ln(\mathcal{H}) \frac{dq_t}{dt}, \qquad (9)$$

FIG. 1. Two adjacent heat cycles of an axisymmetric, steady hurricane. Cycle 1 is defined as A–B–C–D–A, and cycle 2 is defined as A–B′–C′–D–A.

where T is temperature, p is pressure, q is the vapor mixing ratio, q_t is the total water mixing ratio, α is the specific volume, c_{pd} is the specific heat capacity of dry air, c_l is the heat capacity of liquid water, L_v is the latent heat of vaporization, R_v is the gas constant for water vapor, and $\mathscr{H}$ is the relative humidity. The last term in Eq. (9) is an irreversible source of entropy. Note that we neglect the ice phase here; including it would add terms related to thermodynamically irreversible ice-phase effects such as supercooling. By taking the dot product of the vector momentum equation with the three-dimensional velocity vector, we obtain a relationship for the kinetic energy:

$$\frac{d}{dt}\left(\frac{1}{2}|\mathbf{V}|^2\right) = -\alpha\frac{dp}{dt} + \mathbf{V}\cdot\mathbf{F} - wg, \qquad (10)$$

where $\mathbf{V}$ is the three-dimensional velocity, w is its vertical component, g is the acceleration of gravity, and $\mathbf{F}$ is the frictional source of momentum. Eliminating pressure p between Eqs. (9) and (10) yields

$$T\frac{ds}{dt} = \frac{d}{dt}\left[(c_{pd} + c_l q_t)T + L_v q + (1 + q_t)\left(\frac{1}{2}|\mathbf{V}|^2 + gz\right)\right]$$
$$- \mathbf{V}\cdot\mathbf{F} - \frac{dq_t}{dt}\left[R_v T\ln(\mathscr{H}) + \frac{1}{2}|\mathbf{V}|^2 + gz\right]. \qquad (11)$$

We next integrate Eq. (11) around either A–B–C–D–A or A–B′–C′–D–A to obtain

$$\oint T\frac{ds}{dt} = -\oint\mathbf{V}\cdot\mathbf{F} - \oint\frac{dq_t}{dt}\left[R_v T\ln(\mathscr{H}) + \frac{1}{2}|\mathbf{V}|^2 + gz\right]. \qquad (12)$$

The first term on the right side of Eq. (11) is a perfect derivative and thus integrates to zero around a closed loop. If we apply Eq. (12) first to the loop A–B–C–D–A and subtract that from its application to A–B′–C′–D–A, we get a closed integral around the loop B′–B–C–C′–B′:

$$\oint_{\text{inner}} T\frac{ds}{dt} = -\oint_{\text{inner}}\mathbf{V}\cdot\mathbf{F} - \oint_{\text{inner}}\frac{dq_t}{dt}\left(\frac{1}{2}|\mathbf{V}|^2 + gz\right); \qquad (13)$$

$\ln(\mathscr{H})$ is not present as the inner loop is taken to be saturated. The last term in Eq. (13) represents the irreversible entropy loss associated with lifting water mass against gravity and changing its kinetic energy. It is quantitatively small compared to the other terms in Eq. (13) and we henceforth neglect it; thus, we will evaluate

$$\oint_{\text{inner}} T\frac{ds}{dt} = -\oint_{\text{inner}}\mathbf{V}\cdot\mathbf{F}, \qquad (14)$$

where the "inner" notation denotes the circuit B′–B–C–C′–B′. We note that B–C and C′–B′ are adiabatic, and we assume that friction is only important in B′–B. [Emanuel (1986) showed that there must also be frictional dissipation in the leg C–C′ associated with a gain of angular momentum, but this will be small if the radius at which this occurs is not too large.] Using classical aerodynamic flux formulas for the sea surface source of enthalpy and sink of momentum, and taking the circuit B′–B–C–C′–B′ to be of infinitesimal width yields

$$\frac{T_s - T_{\text{out}}}{T_s}\left[C_{k10}|\mathbf{V}_{10}|(k_0^* - k_{10}) + C_{D10}|\mathbf{V}_{10}|^3\right] = C_{D10}|\mathbf{V}_{10}|^3, \qquad (15)$$

where $|\mathbf{V}_{10}|$ is now the 10-m wind speed at the radius of maximum winds, the exchange coefficients pertain to

TABLE 1. Summary of the variables bounded, the diagnostic formulas, and the SI definitions for each form of PI.

PI form	Variable	Diagnostic formula	SI Definition
PI_g	V_g	$\mathrm{PI}_g^2 = \dfrac{C_{k10}}{C_{D10}} \dfrac{(T_b - T_{\mathrm{out}})}{T_{\mathrm{out}}}(k_s^* - k_{10})$	$\mathrm{SI}_g = \dfrac{\max(V_g) - \mathrm{PI}_g}{\mathrm{PI}_g}$
PI_a	V	$\mathrm{PI}_a^2 = \mathrm{PI}_g^2 + r_b \eta_b w_b \dfrac{T_s}{T_o}$	$\mathrm{SI}_a = \dfrac{\max(V) - \mathrm{PI}_a}{\mathrm{PI}_a}$
PI_s	$|\mathbf{V}_{10}|$	$\mathrm{PI}_s^2 = \dfrac{C_{k10}}{C_{D10}} \dfrac{(T_s - T_{\mathrm{out}})}{T_{\mathrm{out}}}(k_s^* - k_{10})$	$\mathrm{SI}_s = \dfrac{\max(|\mathbf{V}_{10}|) - \mathrm{PI}_s}{\mathrm{PI}_s}$

10-m altitude, T_s is the surface temperature, T_{out} is the temperature at C–C', k_s^* is the saturation enthalpy of the sea surface, and k_{10} is the enthalpy at 10 m. Rearranging Eq. (15) yields an expression for what we refer to as the surface PI, or

$$\mathrm{PI}_s^2 = |\mathbf{V}_{10}|^2 = \frac{C_{k10}}{C_{D10}} \frac{T_s - T_{\mathrm{out}}}{T_{\mathrm{out}}}(k_s^* - k_{10}). \qquad (16)$$

No assumptions of gradient wind or hydrostatic balance have been made here. Note that the expression for PI_s is almost identical to that for PI_g, the only difference being that T_s appears instead of T_b, in the numerator of the thermodynamic efficiency ratio.

Summarizing the different versions of PI we will be using in this study, PI_s puts an upper bound on the magnitude of the surface winds, PI_a bounds the maximum azimuthal winds, and PI_g bounds the maximum gradient winds. Similarly, we will denote superintensity by SI_s, SI_a, and SI_g representing the amount by which the maximum winds exceed each version of PI. In this paper, superintensity will be computed as a relative, normalized quantity so that, for example, $\mathrm{SI}_s = [\max(|\mathbf{V}_{10}|) - \mathrm{PI}_s]/\mathrm{PI}_s$. Hereafter, $|\mathbf{V}_{10}|$ refers to simulation data. Table 1 summarizes the forms of PI that will be evaluated in this paper.

3. Numerical simulations

The simulations in this study are conducted using two axisymmetric models, namely, the Axisymmetric Simplified Pseudoadiabatic Entropy Conserving Hurricane Model (ASPECH; Tang and Emanuel 2012) and CM1, version 19, in an axisymmetric configuration (BR09c). Both models' equation sets conserve mass and internal energy in saturated air and include dissipative heating. Most previous SI studies used CM1, but we add in another model to assess the degree to which superintense behavior may be model dependent. Similarly to RE87, in both models, the radiation is parameterized by a simple Newtonian relaxation of potential temperature to the background, which is capped at $2\,\mathrm{K\,day^{-1}}$ of cooling. For simplicity, surface exchange coefficients

are fixed to $C_{k10}/C_{D10} = 1$ with $C_{D10} = 0.002$ and $C_{k10} = 0.002$. The coefficient C_{D10} is similar to the values used in most models for high wind speeds, but the value of $C_{k10} = 0.002$ resulting from these choices is much higher than that generally considered to be most representative of intense hurricanes ($C_{k10} = 0.0012$). This choice was partly motivated by the desire to simulate high-intensity storms, more likely to exhibit superintensity. The domains are $1500\,\mathrm{km} \times 27\,\mathrm{km}$, with a horizontal grid spacing of 2 km for the inner 300 km stretching to 8 km at the edge of the domain. The vertical grid spacing is 300 m for the lower 15 km, stretching to 500 m at the top of the domain in ASPECH, and is uniformly 300 m in CM1. This resolution, lower than has been used for the CM1 simulations in BR09a, was chosen for ease of comparison with ASPECH, a somewhat computationally slower model.

The initial vortex, in both simulations, is defined to have a maximum wind speed of $15\,\mathrm{m\,s^{-1}}$ at a height of 1 km and a radius of 100 km. The vertical extent of the vortex is 15 km, and the radius of zero winds is 500 km. The microphysical parameterization used in both models is the simple liquid water scheme used in RE87 with a terminal velocity of $v_t = 7\,\mathrm{m\,s^{-1}}$. BR09c showed that hurricane maximum intensity is very sensitive to terminal velocity and that $v_t = 7\,\mathrm{m\,s^{-1}}$ yields intensities similar to (but somewhat lower than) the pseudoadiabatic limit. Unless specified otherwise, the asymptotic vertical mixing length is $l_v = 100\,\mathrm{m}$. To ensure that conditional instability is small, the simulations are initialized with the RE87 sounding made available by George Bryan,[1] which is essentially neutral. The sea surface temperature T_s is 27°C in all simulations, with an initial air–sea temperature difference at 10 m of about 3.5°C.

a. Sensitivity studies

The goal of the sensitivity analysis is to push the models from a state where the simulated intensities (gradient, azimuthal, and surface winds) do not reach

---

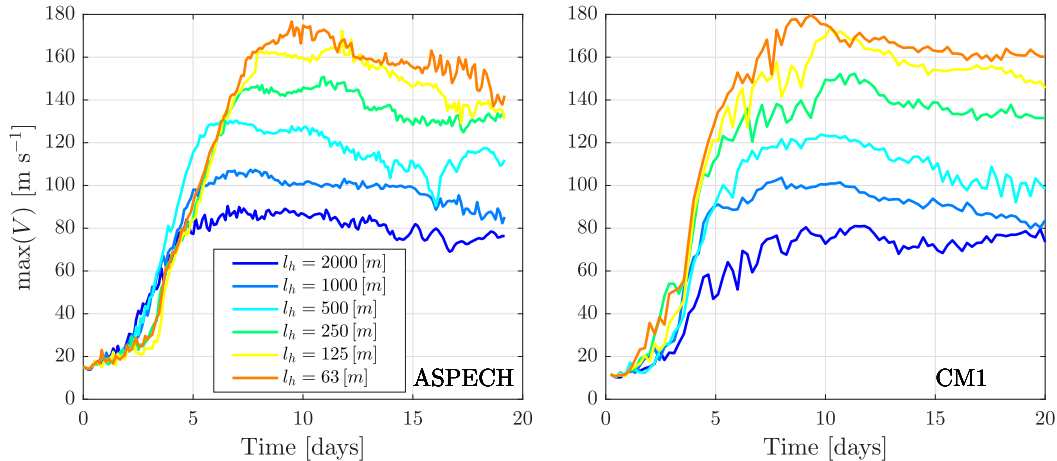[1] http://www2.mmm.ucar.edu/people/bryan/cm1/soundings/input_sounding_rotunno_emanuel.

FIG. 2. Time series of the maximum azimuthal wind *V* in (left) ASPECH and (right) CM1 simulations for all values of l_h (warmer colors correspond to smaller l_h).

their respective PI bounds, to a superintense state. To do so, we decrease the horizontal mixing length l_h by a factor of 2 over each of six simulations from $l_h = 2000$ to 62.5 m. Decreasing l_h decreases the mixing rate of enthalpy and momentum and allows for stronger gradients to form, which in turn leads to more intense hurricanes.

b. In situ estimation of PI

Diagnostics of a given form of PI are realized in situ at the location where the value bounded by that form of PI is maximum. For example, PI_s is computed using Eq. (16) at the radius of maximum surface winds. The thermodynamic disequilibrium is computed as the difference between the surface saturation MSE and the boundary layer MSE, here taken at the first model level (at a height of 150 m). The outflow temperature is taken at the point where the azimuthal velocity changes sign when ascending along a streamline from the PI evaluation point.

4. Results

First, Fig. 2 shows time series of the instantaneous maximum azimuthal velocity for all simulations of the l_h sensitivity experiment and for both models. The time series of both models are qualitatively similar with the exception of an initially faster spinup rate in CM1. Since we are concerned with the steady state only, this does not make much difference in the analysis. Consistent with previous studies (e.g., BR09a; BR09c; Rotunno and Bryan 2012; Bryan 2012), it is clear that as the mixing length decreases, the maximum intensity increases.

Next, in Fig. 3, we show again the ASPECH maximum azimuthal velocity time series for $l_h = 2000$ m and

$l_h = 63$ m alongside time series of diagnosed PI_g and PI_a for the same simulations. Consistent with BR09a and because of supergradient flow, $max(V) > PI_g$, with the difference increasing at small mixing lengths. Again consistent with BR09a, PI_a clearly represents a much better bound on $max(V)$, as it is barely exceeded, even at small l_h. The difference between $max(V)$ and PI_g in Fig. 3 represents the definition of SI used in previous studies. Again, here we aim at comparing PI bounds against the appropriate quantity, so that we define $SI_g = [max(V_g) - PI_g]/PI_g$, the superintensity with respect to the gradient wind PI.

BR09a showed that gradient winds computed from the radial momentum equation in low-mixing TCs tend to be overestimated since the pressure gradient includes a perturbation due to the unbalanced wind contribution. This computation will thus also overestimate SI_g. Throughout this paper, V_g will instead be computed using BR09a's Eq. (16) [Emanuel's (1986) Eq. (11)]:

$$r^2\big|_{M_g} = -M\left[\frac{ds}{dM}(T - T_{out})\right]^{-1}, \qquad (17)$$

where the variables on the right-hand side are taken along the angular momentum surface passing through the position of maximum winds. The radius computed on the left-hand side can then be considered as the radius this angular momentum surface would have if it were actually balanced. The velocity of air with the same angular momentum as that of the maximum winds, and located at a radius $r\big|_{M_g}$, is then the gradient wind.

This method avoids accounting for the unbalanced wind contribution but requires assuming hydrostatic balance and moist slantwise neutrality above the boundary layer,
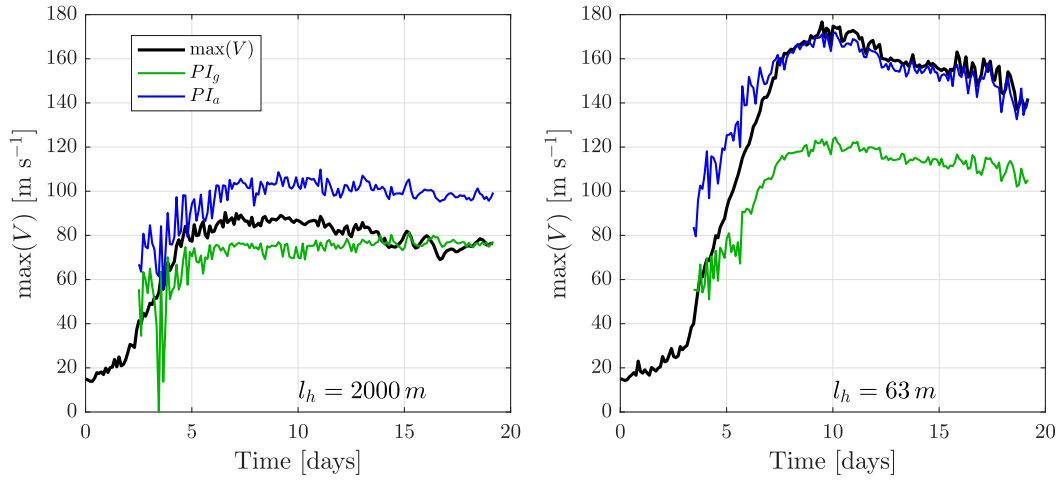
FIG. 3. Time series of the maximum azimuthal velocity, max(V) (black); the gradient PI, PI$_g$ (green); and the azimuthal potential intensity, PI$_a$, (blue) for l_h = (left) 2000 and (right) 63 m. Simulated using ASPECH.

which may impact the resulting V_g as well as SI$_g$. Indeed, moist slantwise neutrality is not respected as well at large values of l_h as it is at small values. More precisely, ds^*/dM decreases with height because of horizontal mixing (not shown), so that V_g is overestimated when l_h is large.

a. Simplifying approximations in PI$_g$ and PI$_a$

The validity of the main physical assumptions of the gradient PI theory, namely, thermal wind balance, moist slantwise neutrality, and the boundary layer closure, has been evaluated in BR09a. In a replication of BR09a's results, we verified that the moist slantwise neutrality and boundary layer closure are fairly well satisfied in the simulations presented here and as such will not discuss them further. However, the simplifying approximations for PI$_g$ and PI$_a$ that allow one to go from Eq. (6) to Eq. (7) have not been evaluated for various intensities. The PI$_g$ derivation approximates $T_s \approx T_b$ for the purpose of computing thermodynamic efficiency, $V_{10} \approx V_{g,b}$ and $\bar{r} \approx r_b$ to relate momentum at the top and bottom of the boundary layer, and $|\mathbf{V}_{10}|^2 \approx V_{g,b}^2$ for the dissipative heating. These approximations are generally thought to be small and largely cancel out. To verify this, we compare the average value of the approximate PI$_g$ to that of the unapproximated form of Eq. (6). The averaging is done over the most intense part of the simulations, from days 8 to 12, corresponding to the times at which we intend to evaluate superintensity. The contribution of each individual assumption to the final result is also evaluated.

Figure 4 shows the mean of the normalized difference between PI$_g$ and unapproximated gradient PI as a function of the mixing length. All results represent the relative departure from the unapproximated form due to a given assumption. For example, the temperature assumption plot (green profile) is really just $(T_s - T_b)/T_b$. The assumptions are multiplicative so that the combined effect of all the approximations (black profile) is not equal to the sum of the individual approximations. Note that while the errors owing to the assumptions about velocities, radius, and dissipative heating can be as large as 20%, they end up cancelling for the most part, so that PI$_g$ is within 10% of the unapproximated PI. This difference is even smaller (about 5%) at small mixing lengths, so that for the purpose of evaluating superintensity, we will use the
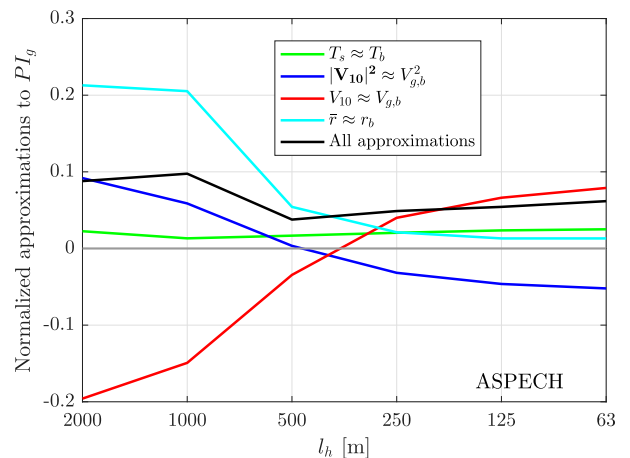

FIG. 4. Contribution of simplifying assumptions to PI$_g$ as a function of l_h, in ASPECH, for the SST approximation (green), the dissipative heating approximation (blue), the exchange coefficient approximation (red), the radius of M surfaces approximation (cyan), and the combined effect of all assumptions (black).
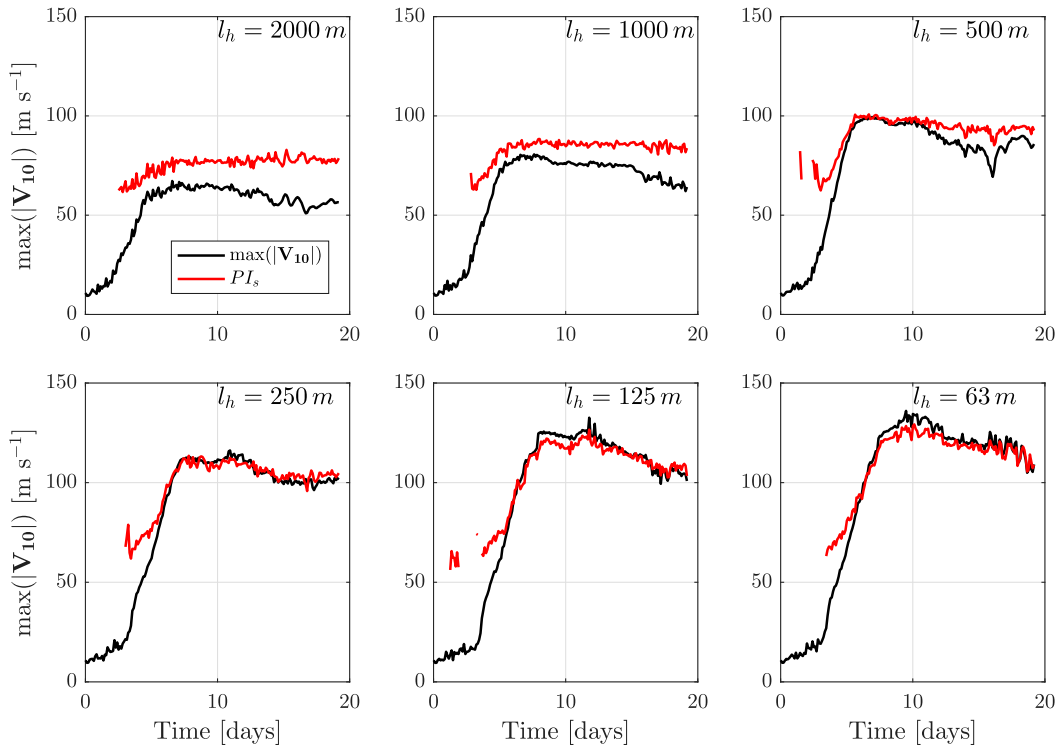
FIG. 5. Time series of the maximum magnitude of surface winds in ASPECH, $|\mathbf{V}_{10}|$ (black; m s^{-1}), and the surface potential intensity, PI$_s$, (red) for all simulations.

approximate PI$_g$ and PI$_a$ forms. In this paper, the approximations described above mostly serve to simplify the interpretation of the PI$_g$ and PI$_a$ forms. However, computing an a priori gradient wind PI from only environmental variables would require taking a similar set of approximations.

b. Surface PI

Next, we look at whether the surface PI (PI$_s$) is well respected in the ASPECH simulations. Contrarily to PI$_g$, which needs to be compared to gradient wind computed from the simulation data, PI$_s$ is directly compared to output surface winds. As such, assumptions enter only in the derivation of the surface PI, not in the quantity to which it is compared.

Figure 5 shows time series of the maximum surface winds and surface PI for all simulations. The time series of PI$_s$ do not extend to the start of the simulation, because the outflow temperature is not initially well defined. The minimum values of PI$_s$ during intensification are similar for all simulations, which is consistent with the identical environment in all simulations. Note again that PI$_s$ depends on a differential Carnot cycle, and the fact that Hakim (2011) showed that simulated steady state hurricanes do not have a full Carnot thermodynamic cycle does not mean that there is any problem

with the PI$_s$ derivation, as it only requires the inner core portion of the Carnot cycle to be valid.

As $|\mathbf{V}_{10}|$ tends to PI$_s$, both time series covary surprisingly closely, with the increase in PI$_s$ following closely the intensification of $|\mathbf{V}_{10}|$. Variations of $|\mathbf{V}_{10}|$ on time scales of less than a day are also captured by PI$_s$. This interesting result is an indication that the Carnot energetic constraint is consistent with the relation between the dynamics and the thermodynamics of the simulated TCs, even on short time scales. It is not entirely clear why PI$_s$ covaries with $|\mathbf{V}_{10}|$ on short time scales rather than on average, over steady periods as per the assumptions of PI. CM1 yields similar results (not shown), but the surface winds exceed PI$_s$ by up to 7% in the $l_h = 63$ m simulation.

5. Superintensity

First, we present the superintensities for each variable, normalized with respect to the corresponding PI bound, and averaged from day 8 to day 12. For example, for the surface SI, SI$_s$ = (max($|\mathbf{V}_{10}|$) − PI$_s$)/PI$_s$. The interpretation of SI is the following: SI$_s$ = −0.2 for a given simulation means that the average magnitude of the surface winds, during the most intense period, is smaller than PI$_s$ by 20%. Conversely, SI$_s > 0$ means that PI$_s$ is
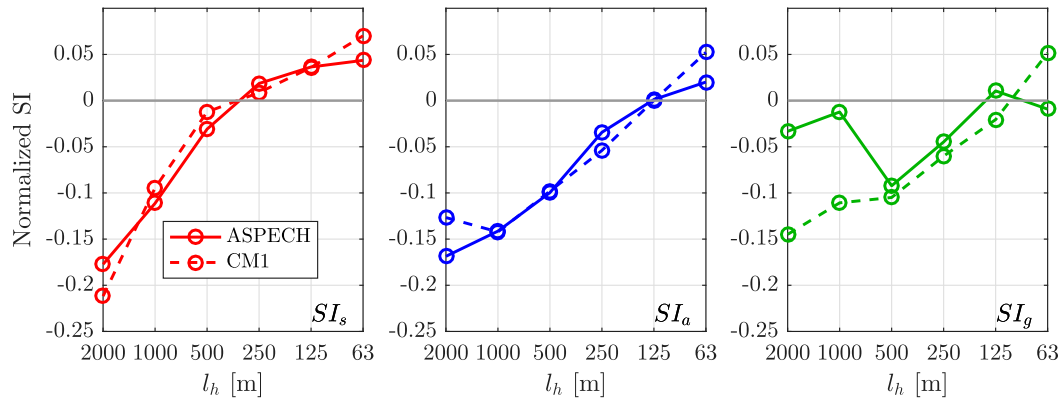
FIG. 6. Averaged normalized SI as a function of (left) l_h with respect to the surface PI, SI_s; (center) the azimuthal PI, SI_a; and (right) the gradient PI, SI_g, for ASPECH (solid) and CM1 (dashed).

exceeded on average during the same period by the quantity it should bound. The same reasoning is applied in computing SI for the azimuthal wind (PI_a) and for the gradient wind (PI_g). Figure 6 shows the various SIs as a function of l_h and for both models.

For most computed superintensities, there is a clear positive tendency with decreasing l_h. In CM1, SI_s increases from about -0.21 to 0.07, SI_a from about -0.17 to 0.05, and SI_g from about -0.15 to 0.05. In ASPECH, SI_s increases from about -0.17 to 0.05, SI_a from about -0.13 to 0.02, and there is no clear trend for SI_g. In both models, SI_s seems to have smaller sensitivities at small mixing lengths. Analyzing SI_g is a bit complicated since the discrepancy (SI_g) between V_g, diagnosed using BR09a's method and PI_g, does not capture the effect of the departure from moist slantwise neutrality and from hydrostatic balance; SI_g, in this case, is due only to the boundary layer assumptions and the simplifying approximations applied between Eqs. (6) and (7).

At this point, it is important to note that the actual intensities and potential intensities vary much more with l_h than does SI. For example, Fig. 3 shows that the peak intensities increase by more than 100% over the range of l_h, while SI_a varies by less than 20% and is generally closer to 0 at small mixing lengths than at large mixing lengths. This tells us that each PI and its bounded quantity both increase and converge with decreasing l_h. This behavior is expected as PI theories are defined for inviscid flow above the boundary layer. Larger mixing lengths imply a decrease in the eyewall entropy gradient so that V_g and V do not reach PI_g and PI_a, respectively. Alternatively, it implies that the assumption of isentropic ascent is not quite satisfied so that $|\mathbf{V}_{10}|$ does not reach PI_s. As l_h decreases, the PI assumptions are better satisfied.

Both models produce similar SI for surface winds. The surface PI diagnostic, PI_s, relies purely on model

thermodynamics, and hence, both models simulate a similar relation among the thermodynamic disequilibrium, the thermodynamic efficiency, and the near-surface winds. The simulations only become superintense with respect to the surface PI at small l_h, with values of $SI_s < 0.05$ in ASPECH and $SI_s < 0.07$ in CM1. Hence, since SI_s remains small at low mixing lengths, we conclude that PI_s is a good bound for surface winds.

The azimuthal wind PI, PI_a, however, depends both on thermodynamic and dynamical diagnosed components. Thus, even if the profiles of SI_a are similar in both models, the ratio of the dynamical and thermodynamic components may not be. Indeed, Fig. 7 shows that the increase in PI_a due to the imbalance [the last term of Eq. (8), divided by PI_a] varies more and reaches larger values in CM1 than in ASPECH. In this study, the sensitivity of SI_a to l_h, which is clearly shown in Fig. 6, is larger than in BR09a, where $SI_a \approx 0$ for all simulations.

The above discrepancy between CM1 and ASPECH may be due to differences between the PBL schemes in both models and to an uncertainty in the computation of the unbalanced contribution. Indeed, here, PI_a is computed by taking in situ values at a single point (point of maximum winds), as should be the case following BR09a. However, at high intensities, the regions of high vorticity η_b and updraft w_b each collapse to one or two grid points that are not necessarily collocated so that diagnosing the contribution of the imbalance yields a somewhat variable effect. We do not, at this point, have an analysis explaining why this is the case but the inaccuracy of the imbalance term may be due to the very large intensities simulated and the relatively low horizontal resolution of the simulations (2000 m in contrast to 1000 m in BR09a). However, PI_a still bounds azimuthal winds within 5% at low mixing lengths.

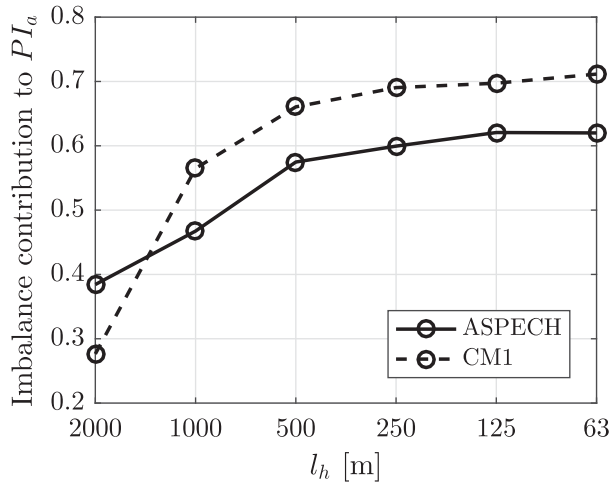The vertical mixing length is also known to be important in controlling the structure and intensity of TCs

FIG. 7. Averaged normalized contribution of the imbalance to PI_a as a function of l_h for ASPECH (solid) and CM1 (dashed).

(e.g., Bryan 2012; Rotunno and Bryan 2012). Thus, to further evaluate the various PI bounds, we performed additional simulations using CM1 for the same values of l_h and for $l_v = 50$, 100 (control), 200, and 400 m. The results are shown in Fig. 8. The SI_a profiles seem to flatten out and shift to higher values (closer to 0 on average) as vertical mixing increases. Interestingly, SI_s profiles seem to have an opposite trends, with the largest superintensities occurring at the smallest vertical mixing lengths. Since we do not yet have a physical understanding of these trends, Fig. 8 is mostly meant to show that the qualitative results of the study are not fundamentally altered by modifying other turbulence parameters.

6. Conclusions

This study introduced a new form of potential intensity bounding the maximum magnitude of the surface winds and based on the idea of a differential Carnot cycle. This derivation has the advantage of only requiring the Carnot cycle's assumptions to be valid for the part of the secondary circulation located in the eyewall of the TCs, which is easier to satisfy.

Previous studies showed that supergradient flow is an important contributor to the azimuthal wind speed in superintense cyclones and that a gradient wind bound was not appropriate in that context. From there, we redefined SI as being the state where a quantity bounded by a given form of PI exceeds that bound. We evaluated three forms of PI (and the associated forms of SI): the newly introduced PI_s and the existing PI_a and PI_g, bounding the magnitude of the surface wind, azimuthal wind, and gradient wind, respectively. The corresponding SI, (SI_g, SI_a, and SI_s) were defined as normalized quantities, so that, for example, $SI_a = (V - PI_a)/PI_a$.

The derivation of PI_g requires making a series of approximations so that its computation only depends on thermodynamic variables. These approximations, namely $T_s \approx T_b$, $V_{10} \approx V_{g,b}$, $\bar{r} \approx r_b$, and $|\mathbf{V}_{10}|^2 \approx V_{g,b}^2$, were shown to cancel out to within 10% for l_h varying from 2000 to 63 m.

SI_g and SI_a are always less than 5%, so that PI_g and PI_a seem to be good bounds on the maximum azimuthal winds, as was shown by BR09a. Finally, SI_s is generally less than 5%, suggesting that the Carnot analog to the derivation from dynamical principles represents a good bound on the surface winds. Even if PI_g is a proper limit for gradient wind, it applies only to gradient wind, an ideal construct that is not necessarily realized. While PI_a applies to an actual wind speed and is very useful in assessing the contribution of supergradient flow to azimuthal winds, its computation relies on dynamical diagnostics. PI_s on the other hand, is a straightforward
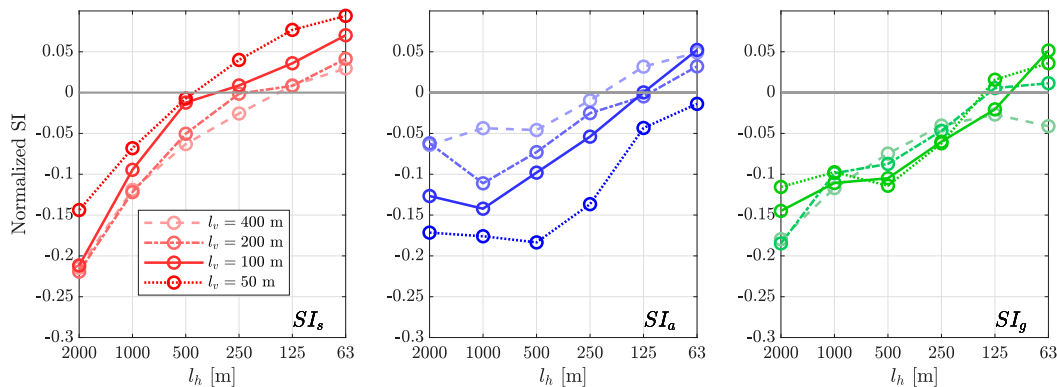

FIG. 8. Averaged normalized SI in CM1 as a function of l_h with respect to (left) the surface potential intensity, SI_s; (center) the azimuthal potential intensity, SI_a; and (right) the gradient PI, SI_g, for all values of l_v (brighter colors indicate lower values of l_v).

thermodynamic bound on surface winds, a quantity that is more relevant to hurricane risk assessment.

Future research directions may include investigating the sensitivity of superintensity to the numerical methods by modifying the scheme used in a given model. It would also be interesting to include a simple boundary layer model in a dynamical PI a priori method to estimate the unbalance in the boundary layer, and to estimate the maximum azimuthal wind for a given environment.

REFERENCES

Bister, M., and K. A. Emanuel, 1998: Dissipative heating and hurricane intensity. *Meteor. Atmos. Phys.*, **65**, 233–240, https://doi.org/10.1007/BF01030791.

Brown, B. R., and G. J. Hakim, 2013: Variability and predictability of a three-dimensional hurricane in statistical equilibrium. *J. Atmos. Sci.*, **70**, 1806–1820, https://doi.org/10.1175/JAS-D-12-0112.1.

Bryan, G. H., 2012: Effects of surface exchange coefficients and turbulence length scales on the intensity and structure of numerically simulated hurricanes. *Mon. Wea. Rev.*, **140**, 1125–1143, https://doi.org/10.1175/MWR-D-11-00231.1.

——, and J. M. Fritsch, 2002: A benchmark simulation for moist nonhydrostatic models. *Mon. Wea. Rev.*, **130**, 2917–2928, https://doi.org/10.1175/1520-0493(2002)130<2917:ABSFMN>2.0.CO;2.

——, and R. Rotunno, 2009a: Evaluation of an analytical model for the maximum intensity of tropical cyclones. *J. Atmos. Sci.*, **66**, 3042–3060, https://doi.org/10.1175/2009JAS3038.1.

——, and ——, 2009b: The influence of near-surface, high-entropy air in hurricane eyes on maximum hurricane intensity. *J. Atmos. Sci.*, **66**, 148–158, https://doi.org/10.1175/2008JAS2707.1.

——, and ——, 2009c: The maximum intensity of tropical cyclones in axisymmetric numerical model simulations. *Mon. Wea. Rev.*, **137**, 1770–1789, https://doi.org/10.1175/2008MWR2709.1.

DeMaria, M., C. R. Sampson, J. A. Knaff, and K. Musgrave, 2014: Is tropical cyclone intensity guidance improving? *Bull. Amer. Meteor. Soc.*, **95**, 387–398, https://doi.org/10.1175/BAMS-D-12-00240.1.

Emanuel, K. A., 1986: An air–sea interaction theory for tropical cyclones. Part I: Steady-state maintenance. *J. Atmos. Sci.*, **43**, 585–605, https://doi.org/10.1175/1520-0469(1986)043<0585:AASITF>2.0.CO;2.

——, 1994: *Atmospheric Convection*. Oxford University Press, 580 pp.

——, 2000: A statistical analysis of tropical cyclone intensity. *Mon. Wea. Rev.*, **128**, 1139–1152, https://doi.org/10.1175/1520-0493(2000)128<1139:ASAOTC>2.0.CO;2.

——, 2017: Will global warming make hurricane forecasting more difficult? *Bull. Amer. Meteor. Soc.*, **98**, 495–501, https://doi.org/10.1175/BAMS-D-16-0134.1.

——, 2018: 100 years of progress in tropical cyclone research. *A Century of Progress in Atmospheric and Related Sciences: Celebrating the American Meteorological Society Centennial*, *Meteor. Monogr.*, No. 59, Amer. Meteor. Soc., https://doi.org/10.1175/AMSMONOGRAPHS-D-18-0016.1.

Hakim, G. J., 2011: The mean state of axisymmetric hurricanes in statistical equilibrium. *J. Atmos. Sci.*, **68**, 1364–1376, https://doi.org/10.1175/2010JAS3644.1.

Hausman, S. A., 2001: Formulation and sensitivity analysis of a nonhydrostatic, axisymmetric tropical cyclone model. Air Force Institute Of Technology Tech. Rep., 227 pp.

Kepert, J. D., 2006: Observed boundary layer wind structure and balance in the hurricane core. Part II: Hurricane Mitch. *J. Atmos. Sci.*, **63**, 2194–2211, https://doi.org/10.1175/JAS3746.1.

Montgomery, M. T., M. M. Bell, S. D. Aberson, and M. L. Black, 2006: Hurricane Isabel (2003): New insights into the physics of intense storms. Part I: Mean vortex structure and maximum intensity estimates. *Bull. Amer. Meteor. Soc.*, **87**, 1335–1348, https://doi.org/10.1175/BAMS-87-10-1335.

Office For Coastal Management, 2018: Assessing the U.S. climate in 2017. NCEI, https://www.ncei.noaa.gov/news/national-climate-201712.

Pauluis, O. M., and F. Zhang, 2017: Reconstruction of thermodynamic cycles in a high-resolution simulation of a hurricane. *J. Atmos. Sci.*, **74**, 3367–3381, https://doi.org/10.1175/JAS-D-16-0353.1.

Persing, J., and M. T. Montgomery, 2003: Hurricane superintensity. *J. Atmos. Sci.*, **60**, 2349–2371, https://doi.org/10.1175/1520-0469(2003)060<2349:HS>2.0.CO;2.

Rotunno, R., and K. A. Emanuel, 1987: An air–sea interaction theory for tropical cyclones. Part II: Evolutionary study using a nonhydrostatic axisymmetric numerical model. *J. Atmos. Sci.*, **44**, 542–561, https://doi.org/10.1175/1520-0469(1987)044<0542:AAITFT>2.0.CO;2.

——, and G. H. Bryan, 2012: Effects of parameterized diffusion on simulated hurricanes. *J. Atmos. Sci.*, **69**, 2284–2299, https://doi.org/10.1175/JAS-D-11-0204.1.

——, Y. Chen, W. Wang, C. Davis, J. Dudhia, and G. Holland, 2009: Large-eddy simulation of an idealized tropical cyclone. *Bull. Amer. Meteor. Soc.*, **90**, 1783–1788, https://doi.org/10.1175/2009BAMS2884.1.

Smagorinsky, J., 1963: General circulation experiments with the primitive equations: I. The basic experiment. *Mon. Wea. Rev.*, **91**, 99–164, https://doi.org/10.1175/1520-0493(1963)091<0099:GCEWTP>2.3.CO;2.

Tang, B., and K. Emanuel, 2012: Sensitivity of tropical cyclone intensity to ventilation in an axisymmetric model. *J. Atmos. Sci.*, **69**, 2394–2413, https://doi.org/10.1175/JAS-D-11-0232.1.

Willoughby, H. E., 1990: Gradient balance in tropical cyclones. *J. Atmos. Sci.*, **47**, 265–274, https://doi.org/10.1175/1520-0469(1990)047<0265:GBITC>2.0.CO;2.

Yang, B., Y. Wang, and B. Wang, 2007: The effect of internally generated inner-core asymmetries on tropical cyclone potential intensity. *J. Atmos. Sci.*, **64**, 1165–1188, https://doi.org/10.1175/JAS3971.1.